Self-Assembling, Low-Cost, and Modular mm-Scale Force Sensor

Joshua B. Gafford, *Student Member, IEEE*, Robert J. Wood, *Member, IEEE*, and Conor J. Walsh, *Member, IEEE*

***Abstract*— The innovation in surgical robotics has seen a shift toward flexible systems that can access remote locations inside the body. However, a general reliance on the conventional fabrication techniques ultimately limits the complexity and the sophistication of the distal implementations of such systems, and poses a barrier to further innovation and widespread adoption. In this paper, we present a novel, self-assembling force sensor manufactured using a composite lamination fabrication process, wherein linkages pre-machined in the laminate provide the required degrees-of-freedom and fold patterns to facilitate self-assembly. Using the purely 2-D fabrication techniques, the energy contained within a planar elastic biasing element directly integrated into the laminate is released post-fabrication, allowing the sensor to self-assemble into its final 3-D shape. The sensors are batch-fabricated, further driving down the production costs. The transduction mechanism relies on the principle of light intensity modulation, which allows the sensor to detect axial forces with millinewton-level resolution. The geometry of the sensor was selected based on the size constraints inherent in minimally invasive surgery, as well as with a specific focus on optimizing the sensor's linearity. The sensor is unique from the fiber-based force sensors in that the emitter and the detector are encapsulated within the sensor itself. The bare sensor operates over a force range of 0–200 mN, with a sensitivity of 5 V/N and a resolution of 0.8 mN. The experimental results show that the sensor's stiffness can be tuned using a thicker material for the spring layer and/or encapsulation/integration with soft materials. The empirical validation shows that the sensor has the sensitivity and the resolution necessary to discern the biologically relevant forces in a simulated cannulation task.**

***Index Terms*— Force sensor, surgical robotics, haptics, light intensity modulation.**

I. Introduction

INNOVATION in surgical robotics has seen a marked paradigm shift from rigid teleoperative systems towards flexible, cooperative and task-specific implementations [1]. While substantial work has gone into the design and control of such systems [2]–[5], significant challenges arise in developing novel end-effector solutions at the scales required, which ultimately limits the sophistication and widespread applicability of these systems. These challenges arise from a general dependence on conventional meso- or micro-scale manufacturing approaches, which are not optimized to develop fully-integrated assemblies at mm-scales in a cost-effective manner. Furthermore, developing robust distal sensing modalities that can be easily integrated into mm-scale packages proves to be a significant challenge from a manufacturing and assembly perspective, where the need for manual intervention to assemble discrete components can limit the complexity of such devices, as well as their scalability down to the millimeter regime.

Several groups have recognized these challenges and are developing unique solutions to enable distal force sensing for flexible surgical procedures. There has been a lot of interest in recent years, both academically and commercially, in using fiber-based optical force sensing methods (fiber bragg gratings, Fabry-Perot interferometry, or light intensity modulation) for force feedback in catheters and flexible surgical robots [6]–[10] and shape estimation of flexible tooling [11], [12]. In 2014, the *ThermoCool SmartTouch* ablation catheter (BioSense Webster), which employs optical fiber-based techniques to resolve distal forces in 3 axes, achieved FDA-approval to become the very first commercially-available ablation catheter to feature fiber-based force feedback in real-time. Such a development is a pivotal step towards widespread acceptance and adoption of force sensing methodologies in minimally-invasive procedures. While fiber-based sensing offers unprecedented resolution (<mN) in a compact package, the entire device must be designed *around* optical transmission fibers which can occupy valuable space otherwise used for working ports or lumens. In addition, expensive interrogators and signal conditioning equipment are often necessary to convert the signal into a meaningful quantity that can be post-processed. Furthermore, optical fibers are sensitive to deformation which must be compensated for (usually with a biasing fiber) to generate a pure reading of the distal force. With increasing clinical interest in force sensing capabilities on-board very small (<3mm OD) packages, it is important to innovate on this field and pursue novel solutions that can optimize sensitivity and modularity while minimizing cost.

In prior work [13] and [14] we have demonstrated the ability to integrate sensors and mechanisms using a monolithic, printed circuit board inspired manufacturing process. In this paper, we build on our prior work to develop a self-assembling, fully-distal, light-intensity-based force sensor that removes the

Manuscript received June 30, 2015; accepted August 28, 2015. Date of publication September 3, 2015; date of current version December 10, 2015. The associate editor coordinating the review of this paper and approving it for publication was Dr. Sillas Hadjiloucas. *(Corresponding author: Conor J. Walsh.)*

J. B. Gafford is with the John A. Paulson School of Engineering and Applied Sciences, Harvard University, Cambridge, MA 02138 USA (e-mail: jgafford@seas.harvard.edu).

R. J. Wood and C. J. Walsh (corresponding author) are with the John A. Paulson School of Engineering and Applied Sciences, Harvard University, Cambridge, MA 02138 USA, and also with the Wyss Institute for Biologically-Inspired Engineering, Boston, MA 02115 USA (e-mail: rjwood@eecs.harvard.edu; walsh@seas.harvard.edu).

Color versions of one or more of the figures in this paper are available online at http://ieeexplore.ieee.org.

Digital Object Identifier 10.1109/JSEN.2015.2476368

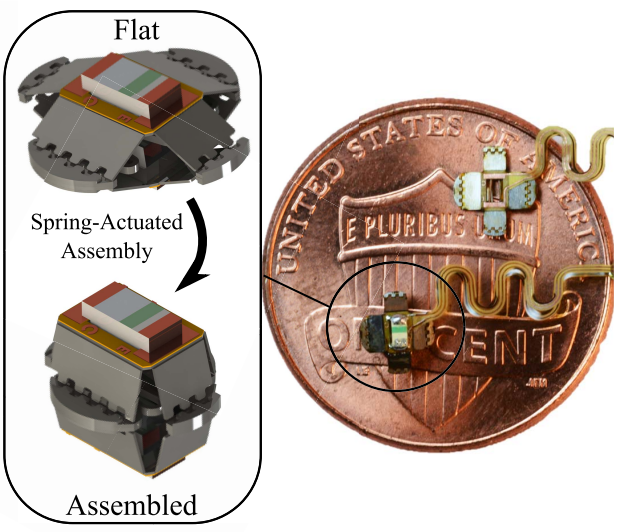

Fig. 1. Fabricated sensors (flat and assembled) on a U.S. penny for scale. Detail shows a photorealisic rendering of the assembly process.

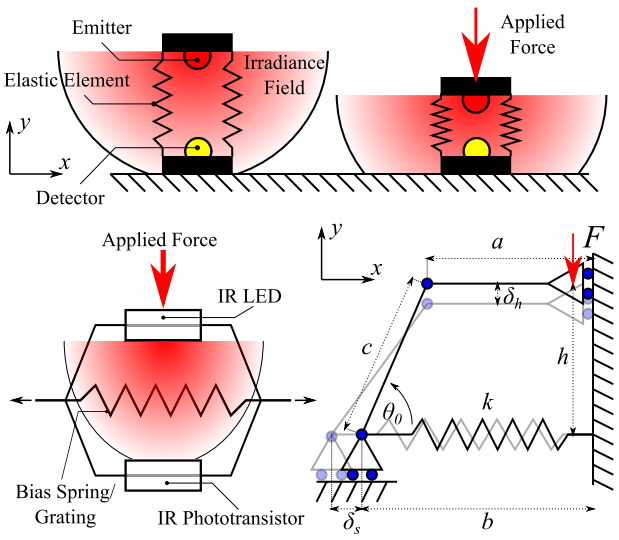

Fig. 2. (top) Point-source model of a light-intensity-modulated sensing system, (bottom left) simplified LIM schematic based on the sensor's intended geometry, (bottom right) simplified mechanical schematic used in the derivation of the sensor's kinematics.

need for optical fiber transmission from a proximal source (Fig. 1). With the emitter and detector contained fully within the distally-integrated sensor, legacy devices can be outfitted with force-sensing capabilities without having to re-design the entire delivery system around the inclusion of optical fibers that must run along the entire length. The absence of fiber transmission results in an extremely stable signal that is not affected by the shape of the delivery system. The ultra-small footprint (2.7mm) means such a sensor could pass through the working port of an 8.6mm endoscope, opening up the possibility of 'sensorizing' electrosurgical tools for intraluminal interventions. The self-assembly property has the opportunity to substantially drive down manufacturing costs by eliminating the need for manual intervention.

This paper begins with a discussion on the theory of operation and presents a mechanical model used to design and optimize the design for linear operation. The sensor is then calibrated and validated in a benchtop environment. To demonstrate the capability of modular integration, the sensor is molded into a mock-up catheter, and force data is recorded in a simulated cannulation task.

II. Theory of Operation

The proposed sensor operates by the principle of *light intensity modulation* (LIM). Consider the simplified schematic shown in Fig. 2 (top). An emitter (modeled as a point source) generates an intensity field which is uniformly spread out over the surface of a hemisphere. A detector is coupled to the emitter by an elastic element. As a force is applied, the elastic element deforms, thereby bringing the emitter closer to the detector. The change in irradiance detected by the detector can be related back to the applied force via an optoelectronic model of the emitter/detector system coupled with a mechanical model describing the elastic element.

The sensor proposed herein is comprised of a monolithically-fabricated hexagonal prism, shown schematically in Fig. 2 (bottom left). Four orthogonal Sarrus linkages couple a top plate and a bottom plate, permitting a pure axial motion between the plates that is co-linear with the sensing axes. An energy source (IR LED) is attached to the top plate, and a detector (IR phototransistor) is attached to the bottom plate. As a force is applied to the top face, the box is 'collapsed', thereby bringing the source closer to the detector by some distance δ_h. This displacement directly correlates to a change in intensity measured by the detector which can be related to the applied force. As the box collapses, an integrated spring provides a reaction force which ultimately determines the 'sensitivity' of the sensor and restores the sensor configuration to its uncollapsed state when the force is removed.

A. Mechanical Model

Consider the mechanical schematic shown in Fig. 2 (bottom right). We ultimately want to determine how much the spacing h changes given a known input force F, which in turn, will allow us to determine the irradiance E_{PT} reaching the phototransistor based on a simple point source model assuming certain assumptions are satisfied. From the geometry of the structure, we observe that only the x component of the applied force goes into stretching the bias spring:

$$F\cos(\theta) = k\delta_s \tag{1}$$

where θ is the hinge angle, k is the spring coefficient and δ_s is the amount of spring deformation. From a purely geometric argument, we can relate θ to other geometric parameters that describe the sensor, as well as the spring stretch δ_s.

$$\theta = \arccos\left(\frac{b+\delta_s-a}{c}\right) \tag{2}$$

Equating Equations 1 and 2, we have:

$$\arccos\left(\frac{k\delta_s}{F}\right) = \arccos\left(\frac{b+\delta_s-a}{c}\right) \tag{3}$$

where a, b and c are geometric variables. Taking the cosine of each side and re-structuring, we are left with an analytical expression for the spring stretch δ_s given an input force F:

$$\delta_s = \frac{F(b-a)}{ck - F} \tag{4}$$

From a geometric argument, we also have:

$$h - \delta_h = c\sin(\theta) \tag{5}$$

where

$$h = \sqrt{c^2 - (b-a)^2} \tag{6}$$

Plugging Equation 4 into Equation 2, we have an analytical expression relating input force F to displacement δ_h.

$$\delta_h = \sqrt{c^2 - (b-a)^2} - c\sin\left(\arccos\left(\frac{b + \frac{F(b-a)}{ck-F} - a}{c}\right)\right). \tag{7}$$

B. Optoelectronic Model

As δ_h is not a directly observable quantity, we need to expand upon the mechanical model to generate an expression for the collector current drained by the phototransistor as a function of the force applied to the sensor. For this, we consider a very simple model, treating the LED as a point source that emits a radiant intensity I_{LED} that is spread out uniformly over the surface area of a hemisphere.[1] The irradiance that strikes the phototransistor is given by the following (simplified) expression:

$$E_{PT} = \frac{I_{LED}}{(h - \delta_h)^2} \tag{8}$$

The quantity I_{LED} is logarithmically related to the LED forward current i_{LED},

$$I_{LED} = \exp(\alpha_1 \log(i_{LED}) + \beta_1) \tag{9}$$

where α_1 and β_1 are specified by manufacturer data sheets. We assume the forward current through the LED is fixed (I_{LED} is constant), and henceforth, we shall treat it as such. The collector current i_{PT} as a function of incident irradiance E_{PT} is similarly exponentially related:

$$i_{PT} = \exp(\alpha_2 \log(E_{PT}) + \beta_2) \tag{10}$$

where α_2 and β_2 are specified by manufacturer data sheets. Putting everything together, our final expression is:

$$i_{PT} = \exp\left(\alpha_2 \log\left(\frac{I_{LED}}{(h-\delta_h)^2}\right) + \beta_2\right) \tag{11}$$

where δ_h is as defined in Equation 7.

[1]This is a suitable approximation so long as the spacing between the emitter and the detector satisfies the 'far-field' condition.

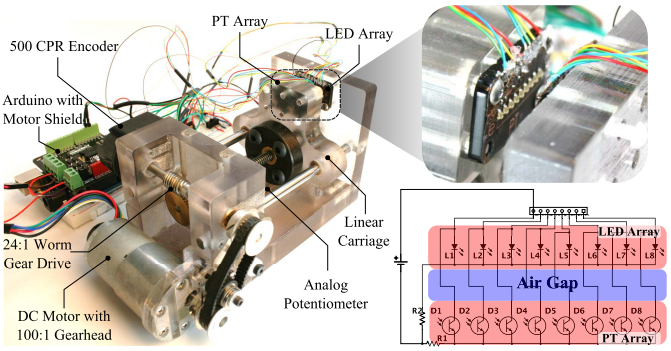

Fig. 3. Sensor calibration hardware, where the inset shows the detail of the phototransistor array, as well as an electrical schematic of the setup.

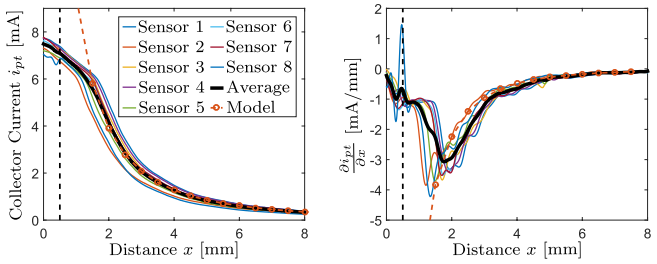

Fig. 4. (left) collector current i_{PT} as a function of distance from the LED source, (right) sensitivity $\partial i_{PT}/\partial x$. The dotted line shows the theoretical far-field cutoff given by the Lambertian simplification.

C. Verification

To experimentally validate the optoelectronic model, a precision positioning system was fabricated to enable the characterization of the phototransistor response as a function of distance from the LED, as shown in Fig. 3. The system features an encoded DC motor with a 100:1 planetary gearhead which transmits motion to a linear carriage attached to a 1/4-20 leadscrew via a worm gear drive which offers an additional 24:1 speed reduction. A 500 counts-per-revolution (CPR) optical encoder is mounted to the worm shaft, giving the system a theoretical positioning resolution of 800 nm barring any backlash within the leadnut. An analog slide potentiometer is attached to the linear carriage for absolute encoding. 10-bit data were captured at a rate of 100 Hz via an Arduino Mega 2560.

An array of eight stationary IR LEDs were aligned with a similar array of phototransistors mounted on the moving carriage. The phototransistor array was moved from absolute minimum distance (saturation) to a distance of 9mm away from the LED array at a constant speed of 125 μm/s. The LEDs and phototransistors were independently addressed to eliminate cross-talk.

Results of this study are shown in Fig. 4. We observe typical far-field behavior that is accurately modeled by a point-source model illustrated in Fig. 2 (top). We also show how the experimental data very accurately matches the optoelectronic model over the far-field regime, but deviates from the model near the Lambertian cutoff ($h/D > 5$, where D is the Lambertian source size of the LED [15]), when the point-source (far-field)

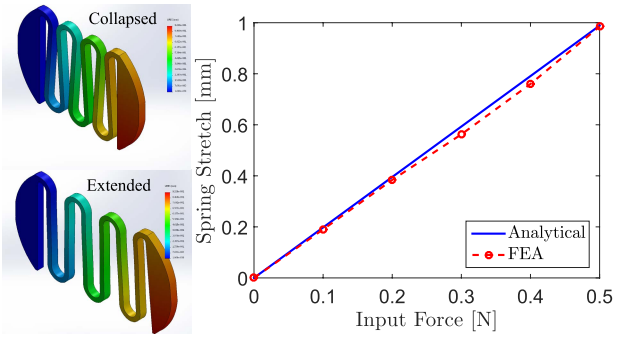

Fig. 5. (a) Representative displacement generated during FEA trials. (b) Comparison between FEA results and the model given by Equation 12.

simplification is no longer a valid assumption.[2] Fig. 4 (left) also shows a peak (roughly constant) sensitivity at between 1.5 and 2mm distance, which is also the regime after which the model is valid. For our design, we will exploit this sweet-spot in an attempt to linearize the behavior while optimizing the sensitivity.

D. Other Linearity Considerations

As is evident in Equation 11, the predicted behavior is highly nonlinear which will lead to special design considerations such that the sensor only operates in the linear regime. The nonlinearities arise from (1) the geometry of the sensor, in which the actual force transmitted to the spring is a function of the cosine of the hinge angle, (2) the exponential dependence of the collector current on the incident irradiance, and (3) the inverse square relationship between irradiance and distance. In order to further guide the design with the added constraint of sufficient linearity, an algorithm was implemented in MATLAB to determine how some aspects of sensor design (namely, half of the initial spacing given by parameter h and spring thickness t_s) affect the force range over which the behavior is 'sufficiently linear' (or, in this case, when the residual of a best-fit line to the curve of i_{PT} vs F is 0.90 or greater). For simplicity of analysis, the stiffness k is modeled as follows:

$$k = \frac{3EI}{NL^3} \tag{12}$$

where E is the Young's Modulus of the material (200 GPa for 304 Stainless Steel), $I = \frac{wt_s^3}{12}$ is the second moment of area of each beam in the serpentine pattern, N is the number of 'switchbacks' in the pattern, and L is the length of each beam in the pattern. To validate this simplification, the model was compared to FEA displacement results performed on a spring with a thickness of 0.006″. The results shown in Fig. 5 demonstrate that the linear simplification is a very good approximation of the behavior.

[2]Note that typical near-field behavior is characterized by a sharp drop to zero output as the separation distance approaches zero. However the LED and phototransistor are hard-molded in 500 μm thick resin which provides an inherent distance offset of 1 mm between the emitter and detector, and as such, the emitter and detector cannot be positioned close enough to exploit this near-field behavior.

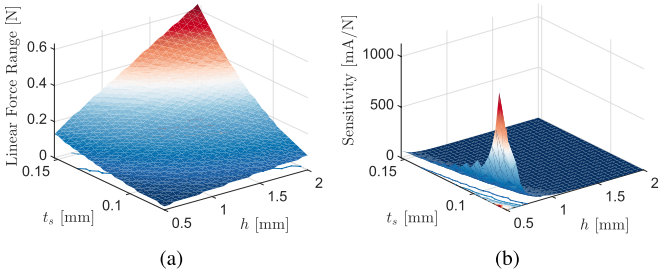

Fig. 6. (a) Parametric analysis of linear range as a function of spring thickness t_s and initial spacing h. (b) Parametric analysis of sensitivity as a function of spring thickness t_s and initial spacing h.

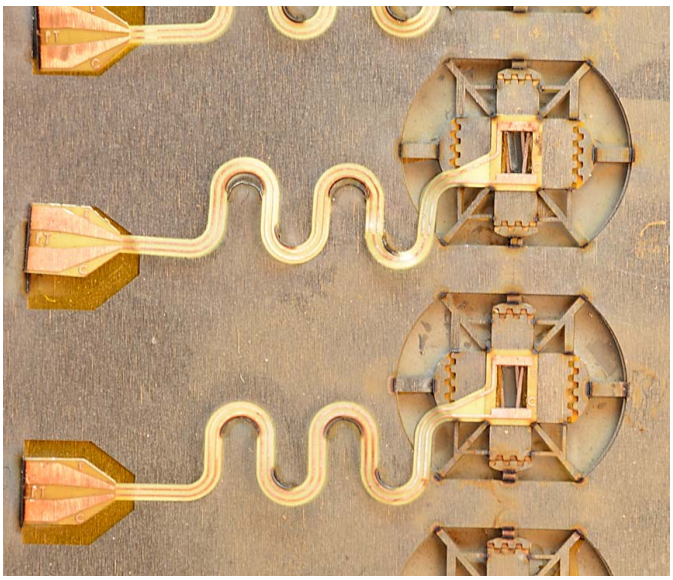

Fig. 7. Batch-fabricated sensors prior to release and self-assembly.

The results of the linearity optimization analysis are shown in Fig. 6. Observe how increasing the spring thickness t_s (and, therefore, the stiffness k) results in the most dramatic increase in linear force range, while reducing the resolution. We also see that the sensitivity $S = \frac{\partial i_{PT}}{\partial F}$ (here it is simply the slope of the best-fit line) drops off substantially by increasing the stiffness and the spacing. Thus there is a significant trade-off between linearity range and sensitivity. Given size constraints and material constraints, we selected an initial sensor spacing of 2 mm (h = 1mm) and a spring thickness of 100 μm. Given these parameters, we should expect decent linearity over 100 mN of applied force. This result will be verified during calibration of the sensor prototype.

III. Fabrication

With the geometry of the sensor determined, the sensor was fabricated using a composite laminate fabrication process called Pop-Up Book MEMS or PCMEMS [16], [17]. Four layers of 304 Stainless Steel comprise the mechanical structure of the sensor. DuPont FR1500 acrylic adhesive joins layers together. Copper-cladded Kapton polyimide is laminated on the top and bottom surfaces to provide electrical contacts for the LED and phototransistor, as well as flex-circuit breakouts for wiring to peripheral architectures.

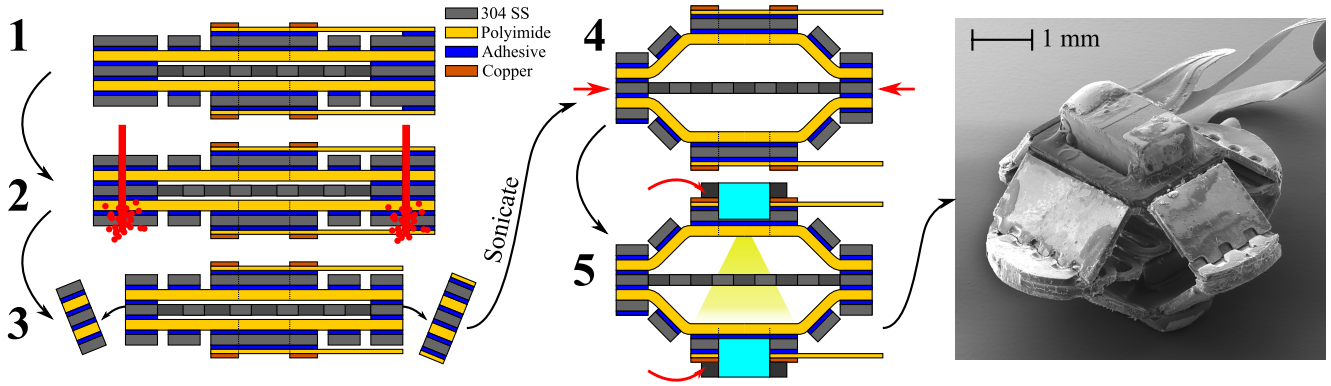

Fig. 8. Release and self-assembly of sensor: (1) laminate after curing, (2) release-cuts made with DPSS laser to release the structure and remove the constraints on the spring, (3) discarding the alignment scaffold, (4) submerge in an ultrasonic bath (agitation causes the spring to overcome the kinematic singularity, thereby retracting and assembling the structure, and (5) pick-and-place LED and PT.

A. Initial Processing

Individual material layers are machined using a diode-pumped solid-state (DPSS) laser. Traces are manufactured on the Copper-cladded Kapton layers using a direct-write photolithography process. The surfaces of each layer are treated using an Argon plasma etching process to promote adhesion, and the layers are placed into an alignment jig laminated together using heat and pressure. Prior to the lamination process, the spring layer is pre-stretched when placed into the alignment jig. The curing process serves to lock the spring into a stretched configuration via adhesion to adjacent layers. Fig. 7 shows what the sensor batch looks like just after the lamination process, prior to release. Sacrificial ribs suspend the sensor body within the alignment scaffold, allowing for easy removal after release cuts are made. The pre-stretched spring can be seen through the 'window' where the LED will be pressed into.

B. Release and Self-Assembly

Release cuts are performed in the DPSS laser to sever the sensor's connection to the alignment scaffold by cutting through the sacrificial ribs. Once release cuts are made, the spring is no longer constrained and is free to retract under its own elasticity; however, a kinematic singularity prevents the spring from retracting and assembling the mechanism in the flat state (the spring restoring force is in line with the neutral axes of the flexural joints). To overcome this singularity, released sensors are submerged in an ultrasonic bath of isopropyl alcohol, which provides the agitation required (and has the added benefit of ridding the sensor of any debris/residue left over by the release cut operation). Once the spring is able to snap past this singularity, it retracts and assembles the sensor into its 3-dimensional shape. Cutouts and fiducials in the laminate allow for the LED and phototransistor to be press-fit into place, where they are reflow soldered to the sensor contact pads. Integrated flex circuitry allows for straightforward wiring to a data acquisition unit. This release process is illustrated in Fig. 8.

C. Molding and Integration

The sensor was integrated into a dummy catheter by means of a molding process. Three-part molds which contain alignment features for locating the sensor and catheter tube in space were 3D-printed (Fig. 9). The sensor was press-fitted into the mold, and a small bead of UV-cure epoxy was applied to temporarily fixate the sensor to the catheter. Sensor electrical traces were routed outside of the mold. The mold was filled with a pre-degassed low durometer silicone rubber (EcoFlex 00-50, Smooth-On, Easton, PA) which is translucent to IR light. After sufficient curing time, the molded catheters are released from the mold. Fig. 10 shows the sensorized catheter after release.

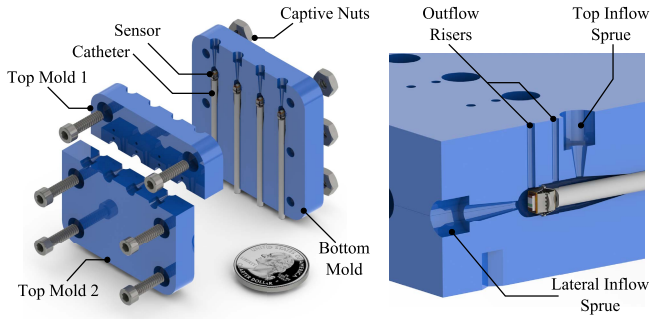

Fig. 9. Mold detail for sensor encapsulation and integration onto a 2mm (6 French) catheter.

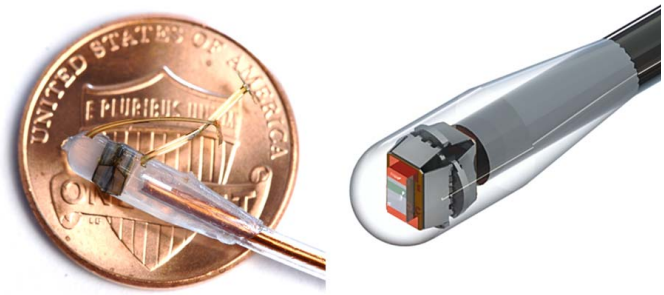

Fig. 10. (left) Image of the sensor encapsulated into the catheter with a U.S. penny for scale, and (right) a photorealistic rendering of the molded system.

D. Signal Conditioning

Light-based sensing modalities are notoriously susceptible to ambient conditions. Although the IR phototransistor has peak spectrum response to 940 nm wavelength, the spectral bandwidth ranges from 400 - 1100 nm, and as such, the sensor

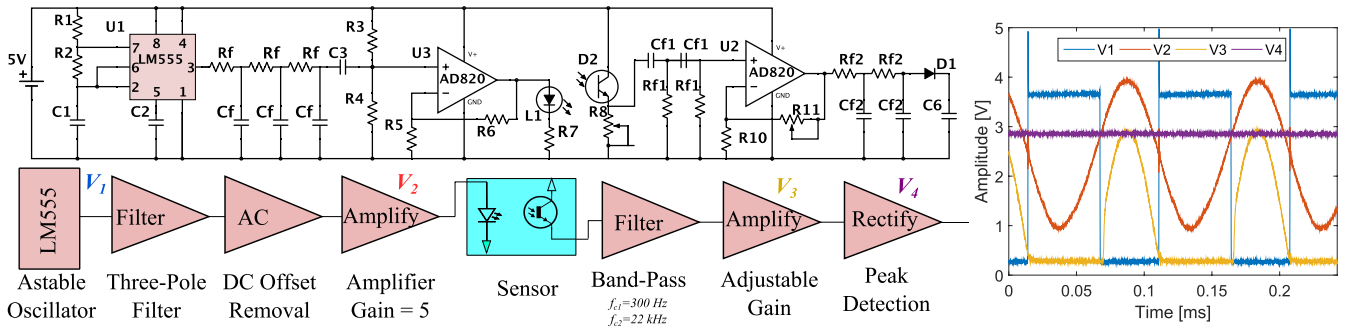

Fig. 11. (left) Electrical architecture the source excitation and filtering of the phototransistor response, and (right) representative scope traces at various locations along the conditioning circuitry.

is sensitive to visible light. To overcome this, we introduce AC-coupling into the conditioning circuitry so that the system only responds to a very narrow band of input frequencies in the temporal domain which are used to drive the LED. This is done as shown in Fig. 11. An LM555 timer, configured as an astable oscillator, provides a square wave with a frequency of $f_{555} = 8kHz$. However, a square wave is not an ideal excitation source due to the high frequency content of the rising/falling edges which are difficult to filter in subsequent stages. To remedy this, the square wave is passed through a three-pole RC filter which produces an approximation of a 8 kHz sine wave with reduced amplitude and an offset of $V_{offset} = 0.5V_{cc}$. This wave is AC-coupled to remove the offset and passed through a non-inverting amplifier to produce a sine wave with 3 V_{pp}. This wave is used to drive the IR LED. The phototransistor collector current is converted into a voltage by a variable resistor R_8, and this voltage is sent through a double-pole band-pass filter with a center frequency at $8kHz$ and a quality factor of $Q = 0.67$ (resulting in a loss of -1.2 dB at 8 kHz). The high-pass and low-pass filter stages within the band-pass filter are buffered by an adjustable-gain non-inverting amplifier. A passive peak detector converts the AC-signal into a DC signal that can be processed by a data acquisition unit. Note that there is an additional low-pass filter inherent in the phototransistor response (with a cutoff of roughly 23 kHz, estimated by $f_c = 0.35/(\tau_r)$ where τ_r is the rise time of the phototransistor (15 μS)). Fig. 11 (right) shows oscilloscope traces of the signal at various locations in the conditioning architecture. We see how the circuit generates a purely-DC analog signal that is modulated according to the input force.

Fig. 12. shows the frequency response of the filtering circuitry to input sinusoids of varying frequency. The data is compared to a model of the theoretical behavior as given by the following transfer function:

$$F(s) = \left(\frac{s}{s + R_{f1}C_{f1}}\right)^2 \left(\frac{R_{f2}C_{f2}}{s + R_{f2}C_{f2}}\right)^2 \left(\frac{\tau_{PT}^{-1}}{s + \tau_{PT}^{-1}}\right) \tag{13}$$

Note that the transfer function also includes a term to account for the inherent low-pass filter contained in the phototransistor response (characterized by the transistor rise-time which is roughly $\tau_{PT} = 15\mu$S). As designed, the pass-band centers at around 8 kHz, and we see that the data matches the

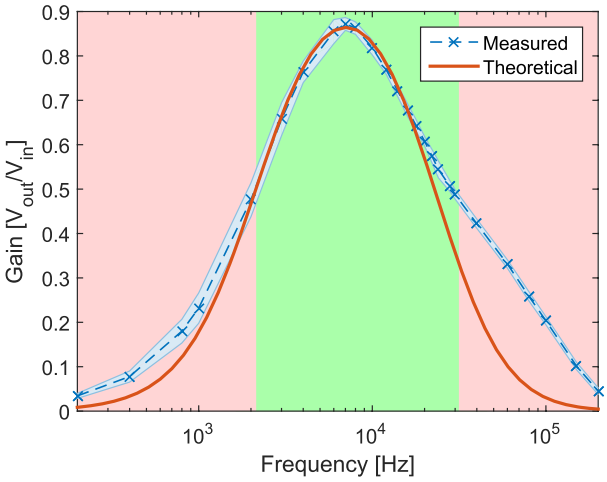

Fig. 12. Measured filter response (plotted against the model) shows predictable behavior within the pass-band (measured $Q = 0.67$).

model quite well near the pass-band, but deviates significantly at higher frequencies. This is likely due to the fact that the phototransistor output no longer resembles a pure sinusoid at higher frequencies, resulting in components that cannot be filtered.

The voltage swing expected from the output of the signal conditioning circuitry, pre-multiplied by the filter attenuation factor of 0.87 as given in Fig. 12, is given by:

$$V_{out} = 0.87\left(1 + \frac{R_{11}}{R_{10}}\right) i_{PT} R_8. \tag{14}$$

IV. Validation

A. Sensor Calibration

The sensor was calibrated by loading the sensor with a reference load-cell (LCL-005 full-bridge thin-beam load cell, Omega Engineering). The calibration curve showing sensor voltage output as a function of input load is shown in Fig. 13(a). As expected, the behavior is quadratic in nature, and the model prediction fits quite well with the observed results. Observe how the behavior is suitably approximated by a linear curve up until about 100 mN of loading, as predicted by the model. The limited range is largely due to the compliance of the bias spring, but since the range is related to the cube of spring thickness, we can custom-tailor

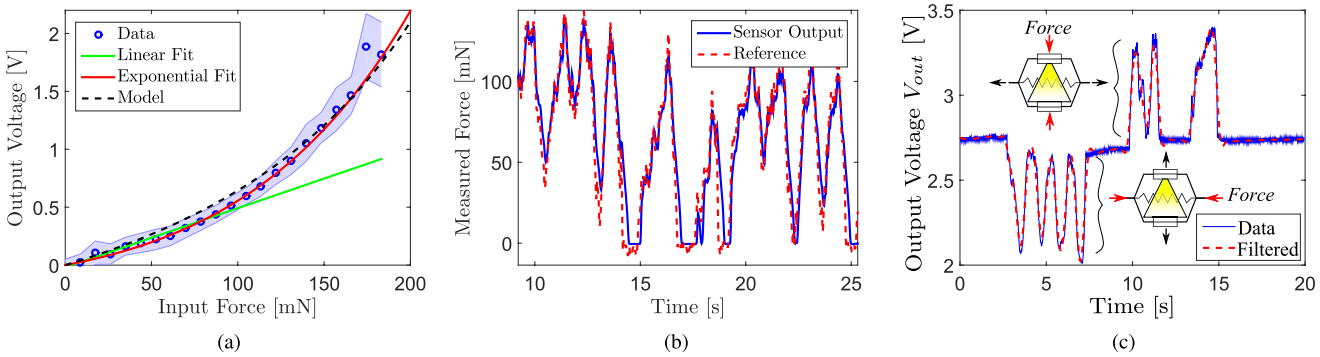

(a) (b) (c)

Fig. 13. (a) Sensor calibration curve, showing a linear fit to the data and a comparison to the model (shaded area shows standard deviation of measurements), (b) sensor response to a dynamic input, compared with a reference signal generated by a load cell, and (c) uncalibrated data showing mounting flexibility.

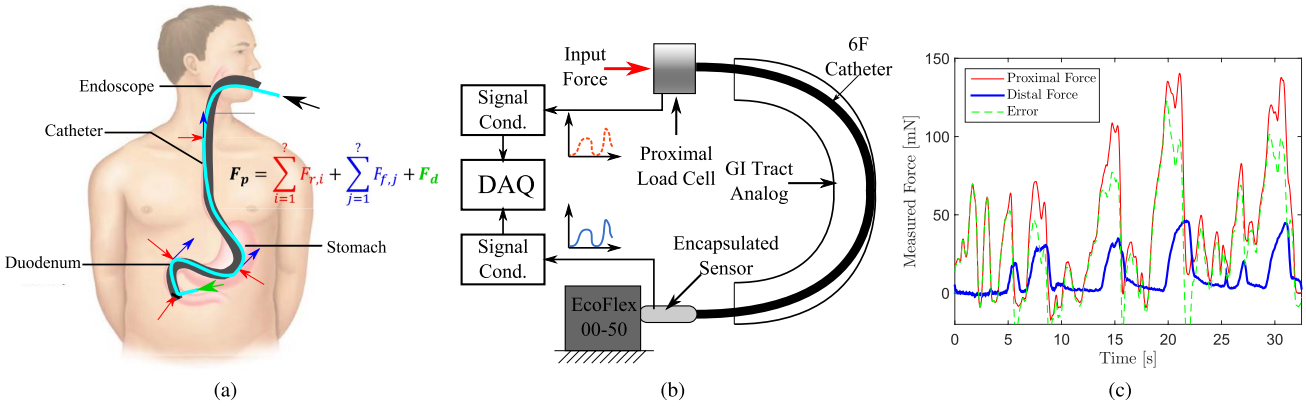

(a) (b) (c)

Fig. 14. (a) Illustration of proximal force corruption by unknown endoscope forces during ERCP, (b) schematic of cannulation simulation, and (c) resulting force profile from palpation, showing substantial disparity between the proximal force and the distal force. The error often exceeds the actual distal force magnitude.

the range/resolution by including thicker spring layers in the laminate. As an example, by using 0.006″ (152 μm) thick 304 SS (as opposed to 0.004″ or 101 μm) for the spring material, we could expect an overall range of around 700 mN (with a linear range of around 350 mN).

The overall sensor calibration curve is well described ($R^2 = 0.99$) by an exponential fit of the following form:

$$F = a\exp(bV_{out}) + c\exp(dV_{out}) \tag{15}$$

For the 0-100mN region, the behavior is suitably approximated ($R^2 = 0.97$) by a linear fit of the following form:

$$F|_{0-100mN} = mV_{out} \tag{16}$$

where $m = 0.0051$ V/mN. The RMS noise of the sensor, found by integrating the power spectral density of a null signal taken over 60 seconds, was found to be 0.8 mN. The resulting signal-to-noise (SNR) over the linear region (from 0 to 100 mN) is 42 dB. Table I summarizes sensor specifications.

Fig. 13(b) shows the prototype sensor tracking a dynamic loading profile, which is simultaneously being tracked by a reference load cell. The linear fit is being used. We see that the sensor is able to accurately track the load over the input force range. Fig. 13(c) shows how the sensor responds to different loading scenarios, demonstrating flexibility in the mounting conditions.

TABLE I
BARE SENSOR PERFORMANCE DATA

Parameter	Value	Unit	%Full-Scale
Sensitivity (0-100 mN)	5.0	V/N	N/A
Range	0-200	mN	N/A
Noise	0.8	mN RMS	0.4
R^2 (Exponential)	0.99	N/A	N/A
R^2 (Linear, 0-100 mN)	0.97	N/A	N/A

B. Cannulation Simulation

Numerous flexible/endoscope-based procedures could benefit from distal sensing capabilities. For example, in endoscopic retrograde cholangeopancreatography (ERCP), wherein the surgeon must position a catheter trans-endoscopically into the bile duct via the duodenal papilla, the surgeon relies solely on proximal haptic cues (and intermittent fluroscopic imaging) to determine whether or not he or she has successfully cannulated the bile duct. However, these proximal forces are grossly contaminated by frictional forces within the endoscope, as well as reaction forces of the endoscope elevation plate, as illustrated in Fig. 14(a). As such, proximal cues present a poor representation of what is actually occurring at the tool-tissue interface. The papilla bifurcates into both the biliary duct and the pancreatic duct, and if the surgeon accidentally cannulates the latter, pancreatitis can occur. With an annual case volume of 445,000 in the United States, and a post-ERCP pancreatitis

rate of up to 17%, there is a significant opportunity to improve outcomes [18]. As such, providing gastroenterologists with a distal 'sense of touch' could allow for greater awareness of the forces being exerted during cannulation.

To replicate this scenario, a bench-level experiment was performed wherein the sensorized catheter was used to probe a tissue analog through a torturous lumens, as shown in Fig. 14(b). A proximal load cell measures the catheter insertion forces, and the distal sensor simultaneously records interaction forces between the catheter tip and a biological tissue analog (EcoFlex 00-50). The results are shown in Fig. 14(c). It is easily observed that the forces felt proximally are very poorly correllated with those actually being applied on the tissue, and are often several times higher. In addition, a phase delay of several seconds indicates poor system controllability. Therefore, there is a real need to explore distal sensing modalities for flexible systems, as the presence of friction and lateral reaction forces along the length of the system makes it impossible to discern the actual distal force from those generated proximally.

V. Conclusion

In this paper, we have presented the design, fabrication and testing of a novel mm-scale uniaxial sensor manufactured using a low-cost, high-throughput, monolithic fabrication technique. Design considerations are presented in detail with the goal of predicting sensor performance *a priori* and optimizing for linearity. The fabrication process is described, and the sensor was calibrated using a reference load cell. To demonstrate modularity, the sensor was molded onto a 6F (2mm) catheter, and a simulated cannulation task was performed to demonstrate the sensor's ability to resolve small (mN) reaction forces at the distal end of a flexible instrument.

Future work will focus on further minimization of the sensor's overall footprint and improving the range. Active actuation strategies will be explored (i.e. integrated balloons) that will enable further tunability and open up the possibility of utilizing the sensor as an actuator with position feedback.

References

[1] M. Aron and M. M. Desai, "Flexible robotics," *Urologic Clin. North America*, vol. 36, no. 2, pp. 157–162, 2009.

[2] P. E. Dupont, J. Lock, B. Itkowitz, and E. Butler, "Design and control of concentric-tube robots," *IEEE Trans. Robot.*, vol. 26, no. 2, pp. 209–225, Apr. 2010.

[3] J. S. Schneider, J. Burgner, R. J. Webster, III, and P. T. Russell, III, "Robotic surgery for the sinuses and skull base: What are the possibilities and what are the obstacles?" *Current Opinion Otolaryngol. Head Neck Surgery*, vol. 21, no. 1, pp. 11–16, 2013.

[4] K. Weaver *et al.*, "The use of teleoperated concentric tube robots for transsphenoidal parasellar surgery," *J. Neurological Surgery, B*, vol. 74, no. S 01, p. A123, 2013.

[5] A. Bajo, L. M. Dharamsi, J. L. Netterville, C. G. Garrett, and N. Simaan, "Robotic-assisted micro-surgery of the throat: The trans-nasal approach," in *Proc. IEEE Int. Conf. Robot. Autom.*, May 2013, pp. 232–238.

[6] I. Iordachita *et al.*, "A sub-millimetric, 0.25 mN resolution fully integrated fiber-optic force-sensing tool for retinal microsurgery," *Int. J. Comput. Assist. Radiol. Surgery*, vol. 4, no. 4, pp. 383–390, 2009.

[7] P. Polygerinos, D. Zbyszewski, T. Schaeffter, R. Razavi, L. D. Seneviratne, and K. Althoefer, "MRI-compatible fiber-optic force sensors for catheterization procedures," *IEEE Sensors J.*, vol. 10, no. 10, pp. 1598–1608, Oct. 2010.

[8] S. Russo, P. Dario, and A. Menciassi, "A novel robotic platform for laser-assisted transurethral surgery of the prostate," *IEEE Trans. Biomed. Eng.*, vol. 62, no. 2, pp. 489–500, Feb. 2015.

[9] H. S. Song, J. W. Jeong, and J. J. Lee, "Optical fiber Bragg grating (FBG) force reflection sensing system of surgical tool for minimally invasive surgery," in *Proc. IEEE 9th Conf. Ind. Electron. Appl. (ICIEA)*, Jun. 2014, pp. 478–482.

[10] P. Puangmali, H. Liu, L. D. Seneviratne, P. Dasgupta, and K. Althoefer, "Miniature 3-axis distal force sensor for minimally invasive surgical palpation," *IEEE/ASME Trans. Mechatronics*, vol. 17, no. 4, pp. 646–656, Aug. 2012.

[11] R. J. Roesthuis, S. Janssen, and S. Misra, "On using an array of fiber Bragg grating sensors for closed-loop control of flexible minimally invasive surgical instruments," in *Proc. IEEE/RSJ Int. Conf. Intell. Robots Syst. (IROS)*, Nov. 2013, pp. 2545–2551.

[12] S. C. Ryu and P. E. Dupont, "FBG-based shape sensing tubes for continuum robots," in *Proc. IEEE Int. Conf. Robot. Autom. (ICRA)*, May/Jun. 2014, pp. 3531–3537.

[13] J. B. Gafford, S. B. Kesner, R. J. Wood, and C. J. Walsh, "Microsurgical devices by pop-up book MEMS," in *Proc. ASME/IDETC Robot. Mech. Med.*, 2013, pp. V06AT07A011-1–V06AT07A011-7.

[14] J. B. Gafford, S. B. Kesner, A. Degirmenci, R. J. Wood, R. D. Howe, and C. J. Walsh, "A monolithic approach to fabricating low-cost, millimeter-scale multi-axis force sensors for minimally-invasive surgery," in *Proc. IEEE Int. Conf. Robot. Autom.*, May/Jun. 2014, pp. 1419–1425.

[15] I. Moreno and C.-C. Sun, "LED array: Where does far-field begin?" in *Proc. SPIE, 8th Int. Conf. Solid State Lighting*, vol. 7058. 2008, pp. 70580R-1–70580R-9.

[16] J. P. Whitney, P. S. Sreetharan, K. Y. Ma, and R. J. Wood, "Pop-up book MEMS," *J. Micromech. Microeng.*, vol. 21, no. 11, pp. 115021-1–115021-7, 2011.

[17] P. S. Sreetharan, J. P. Whitney, M. D. Strauss, and R. J. Wood, "Monolithic fabrication of millimeter-scale machines," *J. Micromech. Microeng.*, vol. 22, no. 5, pp. 055027-1–055027-6, 2012.

[18] M. A. Anderson *et al.*, "Complications of ERCP," *Gastrointestinal Endoscopy*, vol. 75, no. 3, pp. 467–473, 2012.

Joshua B. Gafford received the B.S. degree in mechanical engineering from the Massachusetts Institute of Technology, and the M.S. degree in mechanical engineering from Stanford University. He is currently pursuing the Ph.D. degree at the Harvard John A. Paulson School of Engineering and Applied Sciences. His research focuses on the design of novel surgical end-effectors and systems based on alternative/advanced manufacturing techniques.

Robert Wood (M'01) received the M.S. and Ph.D. degrees from the Department of Electrical Engineering and Computer Sciences, University of California, Berkeley, in 2001 and 2004, respectively. He is currently the Charles River Professor of Engineering and Applied Sciences at the Harvard John A. Paulson School of Engineering and Applied Sciences, and is a Founding Core Faculty Member of the Wyss Institute for Biologically Inspired Engineering, Boston, MA, USA. His current research interests include microrobotics, soft material robots, and bioinspired robotics.

Conor Walsh received the B.A.I. and B.A. degrees in mechanical and manufacturing engineering from Trinity College, Dublin, Ireland, in 2003, and the M.S. and Ph.D. degrees in mechanical engineering from the Massachusetts Institute of Technology, in 2006 and 2010, respectively. He is currently an Assistant Professor of Mechanical and Biomedical Engineering at the Harvard John A. Paulson School of Engineering and Applied Sciences and a Core Faculty Member at the Wyss Institute for Biologically Inspired Engineering, Boston, MA, USA. His current research interests focuses on applying disruptive technologies to the development of robotic devices for augmenting and restoring human performance.